PERGAMON

International Journal of Heat and Mass Transfer 44 (2001) 4433–4443

International Journal of HEAT and MASS TRANSFER

www.elsevier.com/locate/ijhmt

On the discrepancies between theoretical and experimental results for microgravity droplet evaporation

Jeng-Renn Yang, Shwin-Chung Wong *

Department of Power Mechanical Engineering, National Tsing Hua University, Hsinchu 300, Taiwan, Republic of China

Received 2 August 2000; received in revised form 28 February 2001

Abstract

This study aims to solve the discrepancies between the theoretical and experimental results for droplet evaporation. In the literature, all the experiments for microgravity droplet evaporation have been conducted in a hot furnace with the droplet suspended by a fiber. We propose that the discrepancies result from the fact that current theoretical models ignored the conduction into the droplet through the fiber and the liquid-phase absorption of the radiation from the furnace wall. For verification, we formulate a comprehensive model with the effects of fiber conduction and liquid-phase radiative absorption accounted for. For the droplet size variation and evaporation rate constant, good agreement is found between our calculations and the experimental data of H. Nomura, Y. Ujiie, H.J. Rath, J. Sato, M. Kono [Proceedings of 26th Symposium (Int.) on Combustion, 1996, pp. 1267–1273]. Radiative absorption and fiber conduction enhance the evaporation rate significantly. At a low temperature of 470 K, the discrepancies are mainly due to the additional fiber conduction, while at a high temperature of 750 K, the liquid-phase radiative absorption becomes mainly responsible.

Keywords: Droplet; Droplet evaporation; Droplet combustion; Microgravity combustion; Radiative absorption

1. Introduction

Droplet evaporation, being of fundamental importance in extensive engineering applications, have been intensively studied both theoretically and experimentally over the past several decades. Many review papers are available in the literature [1–4]. Most nonconvective droplet evaporation experiments have been conducted at normal gravity [5–8]. The presence of natural convection enhances evaporation slightly for low pressures but strongly for high pressures [7,8]. Recently, droplet evaporation experiments at microgravity have been conducted from atmospheric to supercritical pressures [7–9]. These experiments are important not only for microgravity applications but serve as comparison bases for accuracy test of evaporation models. For nonconvective droplet evaporation under microgravity, the spherical symmetry allows for transient analysis with nonidealized estimation of the thermophysical properties required at elevated pressures [10–16]. In spite of the sophistication, a puzzle remains in that these models predicted much smaller evaporation rates than the experimental data. In the experiments [8,9], droplets with diameter larger than 0.6 mm were tested in an electrically heated furnace. Furthermore, for accurate measurement of the time variation of the droplet size, the droplets were suspended on the tip of a quartz fiber. It is well known that liquid-phase radiative absorption increases with increasing droplet diameter and furnace wall temperature. Therefore, the effects of additional heat input through fiber conduction and the liquid-phase absorption of the radiation emitting from the furnace wall were involved in the experimental data. However, these effects have not been included in the recent comprehensive models [10–16]. Noticing this, it is not surprising to see the significant discrepancies between these theories and experiments.

In the early work for high-pressure droplet evaporation under natural convection, Kadota and Hiroyasu

* Corresponding author. Tel.: +886-3-571-5131; fax: +886-3-572-2840.

E-mail address: scwong@pme.nthu.edu.tw (S.-C. Wong).

0017-9310/01/$ - see front matter
PII: S0017-9310(01)00091-6

Nomenclature

c_P	constant-pressure specific heat
d	diameter
D_{F,N_2}	binary mass diffusivity
f	fugacity
$\Delta H_{v,F}$	enthalpy of vaporization of *n*-heptane
k	thermal conductivity or evaporation rate constant
M	molecular weight
m	total mass of droplet
$-\dot{m}$	droplet evaporation rate
$-\dot{m}''$	droplet evaporation flux
$\dot{Q}_p$	heat input rate from fiber per unit volume
$\dot{Q}_r$	radiative absorption rate per unit volume
$R(t)$	droplet radius
r	spatial coordinate
T	temperature
t	time
v	radial gas velocity
Y	mass fraction

Greek symbols

α	thermal diffusivity
η	dimensionless coordinate in the gas phase
ξ	dimensionless coordinate in the liquid phase
ρ	density
σ	Stefan–Boltzmann constant

Superscripts

l	liquid phase
v	vapor phase

Subscripts

e	environment
f	support fiber
F	fuel
g	gas phase
i	species i
l	liquid phase
m	mean value
r	radiation
0	initial

[17] considered the effects of fiber conduction and liquid-phase radiative absorption in a simplified manner. The fiber conduction was evaluated with a simple one-dimensional steady-state analysis; the radiative absorption was assumed to occur on the droplet surface, adopting an effective surface absorptance whose value appears too small. Although of only qualitative significance, their calculations indicated significant enhancement of the evaporation rate. Shih and Megaridis [18] numerically analyzed the effect of fiber conduction on droplet evaporation under forced convection. For a fiber parallel to the flow direction, only slight enhancement of evaporation was found. In such a configuration, the fiber is in the wake region and subjected to the evaporative cooling. Less heat input through fiber conduction hence resulted. For a cross-flow fiber, stronger effect of fiber conduction is expected. Avedisian and Jackson [19] observed the effect of a support fiber on the soot patterns for droplets burning in a stagnant ambiance in microgravity. With a support fiber, the shell-like soot aggregate forming inside the flame was found to evolve into a nonsymmetric configuration due to the nonsymmetric distribution of thermophoretic and Stefan drag forces around the droplet. This effect is more significant for a larger fiber diameter. They also observed the nonlinearity in the variation of $(d/d_0)^2$ due to the influence of the fiber.

As far as liquid-phase radiative absorption is concerned, many studies assumed that the absorption occurs only on the droplet surface, which is simplified as a black or gray absorber [17,20,21]. Harpole [22] carefully analyzed the reflection, refraction and liquid-phase absorption in the droplet from the incident radiation of black body surroundings by the geometrical-optics approximation. Lage and Rangel [23,24] obtained the total energy absorption distribution inside a liquid droplet by the electromagnetic theory and calculated droplet evaporation accordingly. Their calculated absorptance deviated from Harpole by less than 2% for water droplets with diameter larger than 0.25 mm. As for droplet evaporation, they found that the nonuniformity of the radiation absorption had little effect on the overall droplet heating and evaporation process for their analyzed conditions. The liquid-phase absorption of the soot emission for a burning droplet was investigated by Chiang and Shieh [25].

In this work, we formulate a comprehensive droplet evaporation model in which the fiber conduction and liquid-phase radiative absorption are accounted for, in addition to the inclusion of real-gas thermophysical properties and the variation of the enthalpy of vaporization at elevated pressures. With this model, the predicted evaporation rates are in remarkably better agreement with the experimental data [8,9]. The effects of fiber conduction and radiative absorption will then be examined for different environment temperatures and pressures.

2. Theoretical

The physical problem to be simulated, as in Nomura et al. [9], is illustrated in Fig. 1(a). An *n*-heptane ($T_c = 540.3$ K, $P_c = 27$ atm) droplet (initial diameter of

0.6–0.8 mm) suspended at the tip of a horizontal quartz fiber ($d_f = 0.15$ mm) is evaporating in a hot furnace filled with nitrogen with pressure up to 20 atm. In addition to the heat conduction through the droplet surface, the droplet is subjected to heat inputs through fiber conduction and the liquid-phase radiative absorption of the emission from the furnace wall. In our theoretical model, ambient gas solubility, thermodynamic nonideality, and transience in both the liquid and vapor phases are all included to allow for pressures up to supercritical conditions.

The following assumptions are made in the present model for microgravity droplet evaporation:

1. The system is one-dimensional, spherically symmetric.
2. The pressure is constant everywhere and the momentum equation is unnecessary [11,13–15].
3. Local thermodynamic equilibrium prevails at the liquid/vapor interface.
4. Mass/thermal diffusion of the fuel vapor in the nitrogen is described by the Fick's/Fourier's law.
5. The Soret and the Dufour effect are neglected.
6. Nitrogen solution in the droplet is limited to the droplet surface without penetration into it, due to the small liquid binary mass diffusivity.
7. The emission from the furnace wall is assumed as blackbody radiation at the environment temperature.
8. The gas phase is transparent and the droplet is semitransparent with respect to the incident radiation.
9. The liquid-phase radiative absorption is unaffected by the fiber.
10. Heat input through the fiber is evenly distributed within the droplet volume.

Assumption (1) implies that the weak initial disturbance by generating the droplet on the fiber tip is neglected. Also neglected are the distortion of the droplet shape and the nonsymmetric Stefan flow with the fiber [19]. Assumption (9) should be reasonable because the fiber only occupies 7–20% of the droplet volume before the droplet shrinks to $(d/d_0)^2 = 0.5$. Furthermore, while radiative absorption mainly occurs in the outer layer, most of the fiber volume lies within the inner core of the droplet. Based on these assumptions, the governing equations in both the liquid and the gas phases are as follows.

3. Governing equations

3.1. Liquid phase

Conservation of energy:

$$\rho_l c_{P,l} \frac{\partial T_l}{\partial t} = \frac{1}{r^2}\frac{\partial}{\partial r}\left(k_l r^2 \frac{\partial T_l}{\partial r}\right) + \dot{Q}_r + \dot{Q}_f, \tag{1}$$

where $\dot{Q}_r = -\frac{1}{r^2}\frac{\partial}{\partial r}(r^2 \dot{q}_r)$.

In Eq. (1), $\dot{Q}_r$ and $\dot{Q}_f$ will be calculated using relations to be described later.

3.2. Gas phase

Continuity:

$$\frac{\partial \rho_g}{\partial t} + \frac{1}{r^2}\frac{\partial}{\partial r}(r^2 \rho_g v_g) = 0. \tag{2}$$

Conservation of species:

$$\rho_g \frac{\partial Y_{i,g}}{\partial t} + \rho_g v_g \frac{\partial Y_{i,g}}{\partial r} = \frac{1}{r^2}\frac{\partial}{\partial r}\left(r^2 \rho_g D_{i,g} \frac{\partial Y_{i,g}}{\partial r}\right), \quad i = F, N_2. \tag{3}$$

Conservation of energy:

$$\rho_g c_{P,g} \frac{\partial T_g}{\partial t} + \rho_g c_{P,g} v_g \frac{\partial T_g}{\partial r} = \frac{1}{r^2}\frac{\partial}{\partial r}\left(k_g r^2 \frac{\partial T_g}{\partial r}\right) + \rho_g D_{F,N_2}(c_{P,F} - c_{P,N_2}) \frac{\partial Y_{F,g}}{\partial r}\frac{\partial T_g}{\partial r}. \tag{4}$$

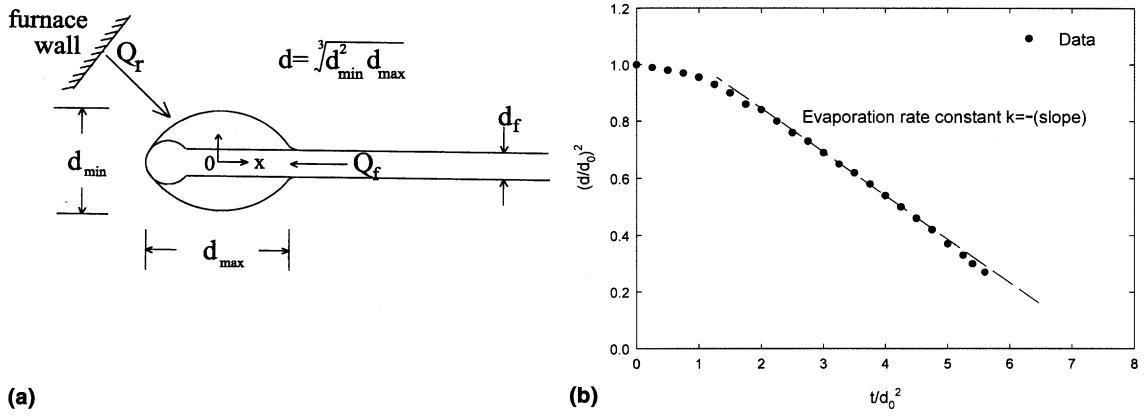

Fig. 1. (a) Schematic of the physical problem. (b) Definition of the evaporation rate constant k.

Equation of state: the Redlich–Kwong–Soave equation of state [26].

4. Initial conditions

At $t = 0$,

$$r \leqslant R(t) : T_{\mathrm{l}} = T_0, \tag{5}$$

$$r > R(t) : T_{\mathrm{g}} = T_{\mathrm{e}}, \quad Y_{\mathrm{F,g}} = 0, \quad Y_{\mathrm{N_2,g}} = 1, \quad v_{\mathrm{g}} = 0. \tag{6}$$

5. Boundary conditions

(a) *At the droplet center* ($r = 0$):

$$\frac{\partial T_{\mathrm{l}}}{\partial r} = 0. \tag{7}$$

(b) *At infinity* ($r \to \infty$):

$$v_{\mathrm{g}} \to 0, \quad T_{\mathrm{g}} \to T_{\mathrm{e}}, \quad Y_{\mathrm{F,g}} \to 0, \quad Y_{\mathrm{N_2,g}} \to 1. \tag{8}$$

(c) *At the droplet surface* ($r = R(t)$):

At the droplet surface, thermodynamic equilibrium dictates the equality of the temperature and the fugacity of both phases for each species:

$$T_{\mathrm{l}}|_{r=R(t)^-} = T_{\mathrm{g}}|_{r=R(t)^+}, \tag{9}$$

$$f_{\mathrm{i}}^{\mathrm{l}} = f_{\mathrm{i}}^{\mathrm{v}}. \tag{10}$$

Energy and mass balance for *n*-heptane at the interface are

$$\left(-k_{\mathrm{l}}\frac{\partial T_{\mathrm{l}}}{\partial r}\right)\bigg|_{r=R(t)^-} = \left(-k_{\mathrm{g}}\frac{\partial T_{\mathrm{g}}}{\partial r}\right)\bigg|_{r=R(t)^+} + \sum_{i=1}^{2}\left(-\dot{m}'' Y_{\mathrm{i,g}} - \rho_{\mathrm{g}} D_{\mathrm{i,N_2}}\frac{\partial Y_{\mathrm{i,g}}}{\partial r}\right)\bigg|_{r=R(t)^+} \times \Delta H_{\mathrm{v,i}}, \tag{11}$$

$$\left(-\dot{m}'' Y_{\mathrm{i,g}} - \rho_{\mathrm{g}} D_{\mathrm{i,N_2}}\frac{\partial Y_{\mathrm{i,g}}}{\partial r}\right)\bigg|_{r=R(t)^-} = \left(-\dot{m}'' Y_{\mathrm{i,g}} - \rho_{\mathrm{g}} D_{\mathrm{i,N_2}}\frac{\partial Y_{\mathrm{i,g}}}{\partial r}\right)\bigg|_{r=R(t)^+}, \tag{12}$$

where $-\dot{m}''$, the evaporation mass flux, can be obtained from the total mass balance

$$m = \int_0^R 4\pi r^2 \rho_{\mathrm{l}}\mathrm{d}r = \frac{4}{3}\pi R^3(t)\rho_{\mathrm{l,m}}, \tag{13}$$

or

$$\dot{m} = 4\pi R^2\left(\frac{\mathrm{d}R(t)}{\mathrm{d}t}\rho_{\mathrm{l,m}} + \frac{R(t)}{3}\frac{\mathrm{d}\rho_{\mathrm{l,m}}}{\mathrm{d}t}\right) = 4\pi R^2(t)\dot{m}''. \tag{14}$$

Another relation between the droplet evaporation flux and the droplet surface regression rate is also needed

$$-\dot{m}'' = \rho_{\mathrm{g}}\left(v_{\mathrm{g}} - \frac{\mathrm{d}R(t)}{\mathrm{d}t}\right)\bigg|_{r=R(t)^+}. \tag{15}$$

6. Calculation of radiative absorption input $Q_{\mathrm{r}}(t)$

When the radiation wave passes across the droplet surface, it is refracted with a small portion reflected. The refracted portion passes through the droplet interior and is gradually absorbed by the liquid. If the droplet is small enough, some portion of the wave will penetrate out of the droplet. In this work, we consider the reflection and refraction at the droplet surface and the liquid-phase absorption and emission using the method of geometric optics, which has been shown to be reliable for droplet diameter larger than 0.1 mm [23]. The gas phase is assumed transparent, without participating media between the furnace wall and the droplet surface. Furthermore, the wall can be treated as a blackbody emitter due to its large area. Also, by examining an actual electrical furnace, we found the wall temperature approximated to the environment temperature. Considering the absorption and the emission of the liquid, the radiation heat flux can be written as [27]

$$\begin{aligned}\dot{Q}_{\mathrm{r}} &= -\frac{1}{r^2}\frac{\partial}{\partial r}(r^2 q_{\mathrm{r}}) = -\frac{1}{r^2}\frac{\partial}{\partial r}\left(r^2\int_0^\infty q_\lambda' \mathrm{d}\lambda\right)\\ &= -\int_0^\infty\left(4\pi\kappa_\lambda I_{\lambda\mathrm{b}} - \kappa_\lambda\int_{4\pi} I_\lambda(r,\tilde{\Omega})\,\mathrm{d}\Omega\right)\mathrm{d}\lambda\\ &= -\int_0^\infty\left(4\pi\kappa_\lambda I_{\lambda\mathrm{b}} - 2\pi\kappa_\lambda\int_{-1}^{1} I_\lambda(r,\mu)\,\mathrm{d}\mu\right)\mathrm{d}\lambda\\ &= 2\pi\int_0^\infty \kappa_\lambda I_\lambda(r)\,\mathrm{d}\lambda - 4\pi\kappa_{\mathrm{p}} I_{\mathrm{b}},\end{aligned} \tag{16}$$

where κ_λ is the monochromatic volumetric absorption coefficient, $\kappa_{\mathrm{p}} \equiv (\int_0^\infty \kappa_\lambda I_{\lambda\mathrm{b}}\mathrm{d}\lambda)/I_{\mathrm{b}}$ is the Planck mean absorption coefficient, Ω is the solid angle, $\tilde{\Omega}$ is the beam direction, μ is the cosine of the angle between the direction $\tilde{\Omega}$ of the beam and the extension of the radius vector $\tilde{r}$, and $I_\lambda(r) \equiv \int_{-1}^{1} I_\lambda(r,\mu)\,\mathrm{d}\mu$ is the monochromatic radiation intensity. Required optical constants such as real and imaginary parts of the complex refractive index of *n*-heptane can be obtained from Tuntomo [28]. The absorption term $I_\lambda(r) \equiv \int_{-1}^{1} I_\lambda(r,\mu)\,\mathrm{d}\mu$ can be evaluated in the integral form by Pomraning and Siewert [29]:

$$\begin{aligned}rI_\lambda(r) = &\int_0^R \kappa_\lambda I_{\lambda\mathrm{b}}(x')(E_1(\kappa_\lambda|r-x'|)\\ &- E_1(\kappa_\lambda(r+x')))x'\mathrm{d}x'\\ &+ 2r\int_0^1 I_\lambda(R,-\mu_0(r,\mu))\cosh(\kappa_\lambda r\mu)\mathrm{e}^{-\kappa_\lambda\pi(R,r,\mu)}\mathrm{d}\mu,\end{aligned} \tag{17}$$

where x' is the integration variable, $I_\lambda(R,-\mu_0(r,\mu))$ is the monochromatic radiation intensity at the inner side of droplet surface, and

$$\pi(x',r,\mu)=[x'^2-r^2(1-\mu^2)]^{1/2},$$

$$E_1(x')=\int_1^\infty \mathrm{e}^{-x't}t^{-1}\mathrm{d}t=\int_0^1 \mathrm{e}^{-x'/\mu}\mu^{-1}\mathrm{d}\mu.$$

The above expression of Pomraning and Siewert [29] is modified in our model to account for the refraction of the incident radiation across the droplet surface. When radiation of intensity I_1 travels from the gas with an index of refraction $n_1=1.0$ to the droplet with an index of refraction $n_2>1.0$, the radiation intensity is magnified to $I_2=n_2^2 I_1$. Further, from the Snell's law, when the hemispheric incident radiation passes across the droplet surface, the range of radiation path is concentrated to a cone-like zone with an opening angle of $\cos^{-1}(1-(1/n_2)^2)^{1/2}$. Consequently, the radiative absorption term becomes

$$\begin{aligned} rI_\lambda(r)=&\int_0^R \kappa_\lambda I_{\lambda\mathrm{b}}(x')(E_1(\kappa_\lambda|r-x'|)\\ &-E_1(\kappa_\lambda(r+x')))x'\mathrm{d}x'+2r\int_0^1 n_2^2 I_\lambda\\ &\times(R,-\mu_0(r,\mu))\cosh(\kappa_\lambda r\mu)\mathrm{e}^{-\kappa_\lambda\pi(R,r,\mu)}\mathrm{d}\mu\\ &(\text{when } 0\leqslant r\leqslant r^*,r^*=R/n_2)\end{aligned}$$

or

$$\begin{aligned} rI_\lambda(r)=&\int_0^R \kappa_\lambda I_{\lambda\mathrm{b}}(x')(E_1(\kappa_\lambda|r-x'|)\\ &-E_1(\kappa_\lambda(r+x')))x'\mathrm{d}x'+2r\int_{(1-(r^*/r)^2)^{1/2}}^1 n_2^2 I_\lambda\\ &\times(R,-\mu_0(r,\mu))\cosh(\kappa_\lambda r\mu)\mathrm{e}^{-\kappa_\lambda\pi(R,r,\mu)}\mathrm{d}\mu\\ &(\text{when } r^*\leqslant r\leqslant R). \end{aligned}\tag{18}$$

From above, $I_\lambda(R,-\mu_0(r,\mu))=(1-\rho_\lambda)I_{\lambda\mathrm{b}}$, where $I_{\lambda\mathrm{b}}$ is the monochromatic black-body radiation intensity and ρ_λ is the monochromatic reflectivity, which can be approximated from Özisik [27] with $n_2=1.387$ for *n*-heptane.

Eqs. (16) and (18), derived from geometrical optics, are applied for the liquid-phase radiative absorption. However, since the calculation is lengthy and the present application is for large droplets of 0.7 mm diameter, we further consider the appropriateness of adopting an effective surface absorptance [17,20,21]. For large droplets of hydrocarbons or water, liquid-phase absorption is confined to a comparatively thin subsurface layer. Therefore the absorption may be approximately considered to occur only on the surface with an effective surface absorptance, α_{eff} [23]. The liquid energy equation and the energy balance at the interface become

$$\rho_1 c_{\mathrm{P,l}}\frac{\partial T_\mathrm{l}}{\partial t}=\frac{1}{r^2}\frac{\partial}{\partial r}\left(k_\mathrm{l}r^2\frac{\partial T_\mathrm{l}}{\partial r}\right)+\dot{Q}_\mathrm{f},\tag{1'}$$

$$\begin{aligned}\left(-k_\mathrm{l}\frac{\partial T_\mathrm{l}}{\partial r}\right)\Big|_{r=R(t)^-}=&\left(-k_\mathrm{g}\frac{\partial T_\mathrm{g}}{\partial r}\right)\Big|_{r=R(t)^+}+(-\dot{m}''\Delta H_{\mathrm{v,F}})\\ &+\alpha_{\mathrm{eff}}\times\sigma\left(T_\mathrm{e}^4-T_\mathrm{l}^4\big|_{r=R(t)^-}\right).\end{aligned}\tag{11'}$$

In Fig. 2, comparisons are made for the internal temperature distributions and evaporation rates obtained using the method of geometrical optics and effective surface absorptance, respectively. Fig. 2(a) shows that the simplified consideration with $\alpha_{\mathrm{eff}}=0.93$ yields good approximation for the evaporation rate for different environment temperatures. The value $\alpha_{\mathrm{eff}}=0.93$ agrees with those obtained for *n*-decane droplets ($\alpha_{\mathrm{eff}}\sim 0.92$–$0.94$) for similar droplet diameter and environment temperatures by the electromagnetic theory [23]. The temperature distributions within the droplet at

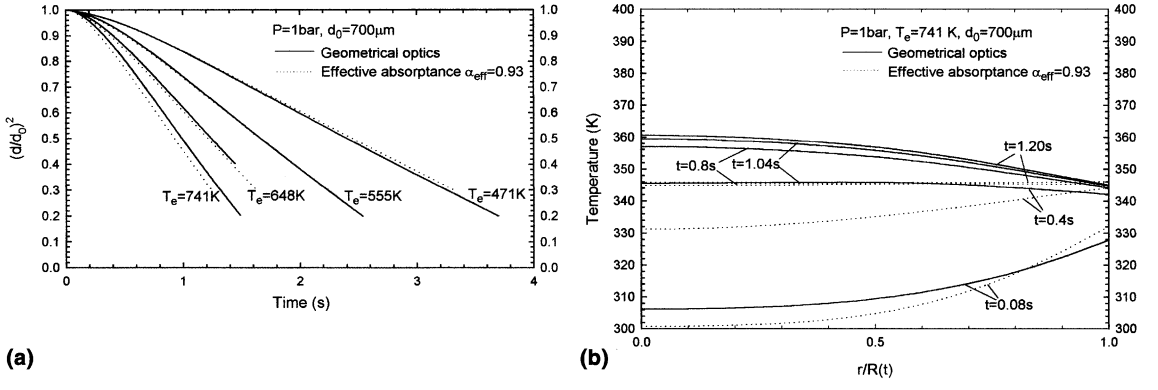

Fig. 2. Results from the method of geometrical optics and effective surface absorptance for: (a) evaporation rate and (b) internal temperature distributions.

different times are compared in Fig. 2(b). For the whole droplet lifetime, the internal temperatures obtained from geometrical optics are higher, with the internal absorption clearly manifested. The differences in droplet surface temperature diminishes gradually. Since our present interest is on the evaporation rate, the approximate method with an effective surface absorptance of $\alpha_{\text{eff}} = 0.93$ is adopted in our subsequent calculations, for the sake of simplicity.

6.1. Calculation of fiber conduction input $Q_{\text{f}}(t)$

To calculate the conduction input through the fiber, we use a transient one-dimensional analysis described as follows.

Since the fiber is fine and the Biot numbers are of the order of $O(10^{-2})$, the temperature distribution in the fiber is assumed to be one-dimensional. Neglecting the absorption of the incident radiation by the fiber, the conservation of energy can be written as

$$\rho_{\text{f}} c_{\text{P,f}} \frac{\partial T_{\text{f}}}{\partial t} = k_{\text{f}} \frac{\partial^2 T_{\text{f}}}{\partial x^2} + \frac{4h_{\infty}}{d_{\text{f}}}(T_{\infty} - T_{\text{f}}). \tag{19}$$

In Eq. (19), h_{∞}, the heat convection coefficient over a horizontal cylinder, is obtained with $h_{\infty} = Nu_{\infty} k_{\infty}/d_{\text{f}}$, where $Nu_{\infty} = 0.36$ for the limiting stagnant situation [30]. For $-R \leqslant x \leqslant R$, the fiber is immersed in the droplet and $h_{\infty} = h_{\text{l},\infty}$; for $x > R$, the fiber is in the gas and $h_{\infty} = h_{\text{g},\infty}$.

$$\begin{aligned} &\text{The initial condition is : } T_{\text{f}}(0,x) = T_0, \\ &\text{The boundary condition at } x \to \infty \text{ is : } \partial T_{\text{f}}/\partial x = 0. \end{aligned} \tag{20}$$

The other boundary condition at the tip of the fiber, where the droplet is positioned, is not readily known. We have tried the following three different options for the boundary condition at the tip:

$$\text{(a) at } x = 0 : \ \partial T_{\text{f}}/\partial x \approx 0, \tag{21a}$$

$$\text{(b) at } x = -R : \partial T_{\text{f}}/\partial x \approx 0, \tag{21b}$$

$$\text{(c) at } x = -R : \ -k_{\text{f}} \frac{\partial T_{\text{f}}}{\partial x} \approx h_{\text{g},\infty}(T_{\text{g}} - T_{\text{f}}). \tag{21c}$$

Since no significant difference is found for them, condition (a) is adopted for its simplicity. The properties of quartz, the fiber material for the experiments [8,9], are $\rho_{\text{f}} = 2.22\ \text{g/cm}^3$, $k_{\text{f}} = 3.29 \times 10^{-3}\ \text{cal/cm s K}$, and $c_{\text{p,f}} = 0.178\ \text{cal/g}$ [31].

With T_{f} solved from Eqs. (19)–(21a), the fiber conduction input can be calculated by

$$\dot{Q}_{\text{f}} = \left(\int_{x=-R}^{x=R} h_{\infty}(T_{\infty} - T_{\text{f}}) \pi d_{\text{f}} \, \text{d}x \right) / V_{\text{net}},$$

where V_{net} is the net volume of the liquid fuel (the fiber volume not included).

In the calculations, the initial droplet diameter d_0 is 0.7 mm. The quartz fiber diameter d_{f} is 0.15 mm, unless specified otherwise.

7. Thermophysical properties and interface considerations

Thermodynamic nonideality in the gas and the liquid phases and the variation of the enthalpy of the vaporization with increasing pressure are carefully calculated, principally as Hsieh et al. [10]. The methods used are briefly described as follows.

Liquid density is determined by the method of Hakinson and Thomson [32] for low pressures and Thomson et al. [33] for high pressure correction. Liquid specific heat follows Daubert and Danner [34]. The method of Latini et al. [26] is adopted for thermal conductivity for low pressures and the method of Latini and Baroncini [26] for high pressures.

Gas-phase thermophysical properties are calculated for *n*-heptane, nitrogen and their mixtures. Gas phase thermal conductivity is calculated following Roy and Thodos [26] for pure *n*-heptane and Daubert and Danner [34] for nitrogen. For thermal conductivity of the mixtures is adopted the Wilke's method [26] for low pressures with high pressure correction by Stiel and Thodos [35]. Gas-phase specific heats of *n*-heptane and nitrogen at atmospheric pressure are obtained from Daubert and Danner [34], with the correction for pressure effect by the method of Lee and Kesler [37]. The gas-phase binary mass diffusivity is calculated us-

Table 1
The methods to evaluate the thermophysical properties

Properties	Method
ρ_{l}	Hankinson and Thomson [32] for low pressures Thomson et al. [33] for high pressure correction
$c_{\text{P,l}}$	Daubert and Danner [34] for low pressures
k_{l}	Latini et al. [26] for low pressures Latini and Barocini method for high pressure correction [26]
k_{g}	Daubert and Danner [34] for k_{N_2} Roy and Thodos [26] for k_{F} Mixing rule for low pressures [26] High pressure correction [35] Extended by Yorizane et al. [36]
$c_{\text{P,g}}$	$c_{\text{P,F}}, c_{P,\text{N}_2}$ for low pressures [34] Mixing rule for low pressures: mass fraction weighting High pressure correction [37]
$D_{\text{F,N}_2}$	Low pressure: Chapman–Enskog method [26] high pressure [38]
$\Delta H_{\text{v,F}}$	Following Hsieh et al. [10] with SRK equation of state

ing the Chapman and Enskog theory [26] for low pressures and the method of Takahashi [38] for high pressures.

The modified Redlich–Kwong–Soave equation of state is adopted to calculate gas density and thermodynamic equilibrium at the droplet surface. As was indicated by Zhu and Aggarwal [16], the modified Redlich–Kwong–Soave and Peng–Robinson equations of state are equally satisfactory. The methods to evaluate the thermophysical properties are summarized in Table 1.

8. Numerical

To account for the droplet surface regression during evaporation, transformations of the spatial coordinates in both the liquid and the gas phases are made to fix the surface. For the liquid phase ($r \leqslant R(t)$), r is changed to $\xi(r,t)$, where $\xi(r,t) = r/R(t)$, $0 \leqslant \xi(r,t) \leqslant 1$. Similarly, in the gas phase ($r \geqslant R(t)$), r is changed to $\eta(r,t)$, where $\eta(r,t) = \ln(r/R(t))$, $0 \leqslant \eta(r,t) < \infty$. The fully implicit scheme backward in time and central in space is used to discretize the governing equations and boundary conditions. In our numerical experimentation, time step $\Delta t = 0.001$ s and grid size $\Delta\xi = \Delta\eta = 0.01$ are adequately small for all of our computations. Infinity is set at 100 times the droplet radius.

When the initial conditions are defined, the thermophysical properties are calculated before solving both liquid- and gas-phase governing equations with boundary conditions. Gas phase continuity is calculated using the Euler predictor-corrector method. Surface temperature, T_s, and droplet evaporation mass flux, $-\dot{m}''$, are solved iteratively with Eqs. (1)–(15) until $|T_s - T_s^0| < 10^{-4}$ or $|(\dot{m}'' - \dot{m}_0'')/\dot{m}''| < 10^{-5}$.

9. Results and discussion

9.1. Preliminary work

To confirm the reliability of our theoretical model and numerical scheme, we have made careful examinations by reproducing various earlier published results [8,12,14,16,39]. The effects of fiber conduction and liquid-phase radiative absorption are temporarily precluded.

First, Hubbard et al. [39] examined the effects of transience and variable properties on the *n*-octane droplet evaporation with constant liquid-phase properties. Although the momentum equation and the pressure variation in space were considered, the nonuniformity of pressure distribution was shown to be less than 0.3% [39]. Also, their model did not account for the nonideality at high pressures. Results of the cases of Hubbard et al. shown in [39, Fig. 1] have been reproduced closely.

Jia and Gogos [12] investigated *n*-hexane droplet evaporation for subcritical to supercritical conditions. They assumed constant pressure and constant liquid properties. Real gas effects in gas phase density and enthalpy of vaporization were considered, with solubility of nitrogen precluded. The cases in [12, Fig. 6] have been also reproduced closely.

Ristau et al. [8] simplified the droplet evaporation analysis by assuming constant liquid properties, ideal thermodynamic properties, constant pressures, and averaged gas-phase thermal conductivity and specific heat. The unsteady gas phase analysis for an *n*-heptane droplet [8, Fig. 5] has been rerun with excellent agreement.

Jiang and Chiang [14] extended the high-pressure evaporation model of Hsieh et al. [10] to calculate the evaporation of the *n*-pentane droplets in a cluster with additional edge-region boundary conditions. Transient in both the liquid and gas phases, their high pressure model included the effect of thermodynamic nonideality, spatial property variation, and ambient gas solubility. Our calculations closely duplicate their numerical results of Fig. 4 and [14, Fig. 11] for dilute spray cases.

We have also compared the phase equilibrium under supercritical pressures for the *n*-heptane/nitrogen mixtures with the results of Zhu and Aggarwal [16, Fig. 1], which match well with the experimental data. The agreement is excellent. Also closely reproduced is the enthalpy of vaporization for *n*-heptane [16, Fig. 2b].

9.2. Comparison with experimental data

Including the effects of fiber conduction and radiative absorption, the evaporation rate from our model will be compared with experimental data of Nomura et al. [9] and Ristau et al. [8], which are the most carefully performed microgravity evaporation experiments available.

The theoretical results of the time variation of the normalized squared droplet diameter are compared with the experimental data [9] in Figs. 3–6, respectively, for pressures of 1, 5, 10, and 20 atm. The experimental data for 50 atm are not included due to the declared unreliability [9]. In each plot we show the calculations with and without the effects of fiber conduction and radiative absorption for different environment temperatures. In Fig. 3, it is shown that ignoring both the effects of fiber conduction and radiative absorption in the calculation leads to the largest under-predictions of the evaporation rate. When both effects are considered, the agreement becomes excellent for all different temperatures. It can also be seen that the relative importance of radiative absorption increases with increasing temperature. These effects are similarly shown for higher pressures in Figs. 4–6. The agreement is also very good for $P = 5$ atm (Fig.

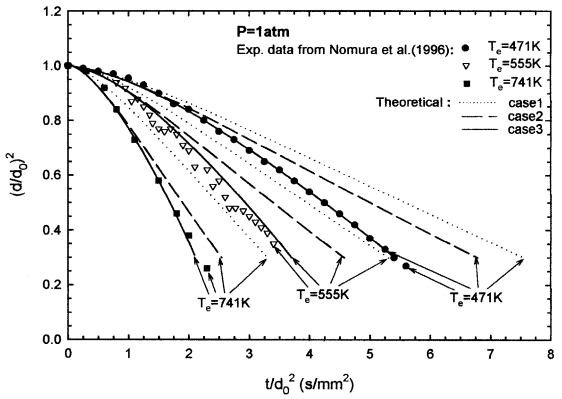

Fig. 3. Theoretical and experimental time variations of normalized squared droplet diameter for different temperatures, $P = 1$ atm. (Case 1: ignoring both fiber conduction and radiative absorption; Case 2: including radiative absorption; Case 3: including both fiber conduction and radiative absorption.)

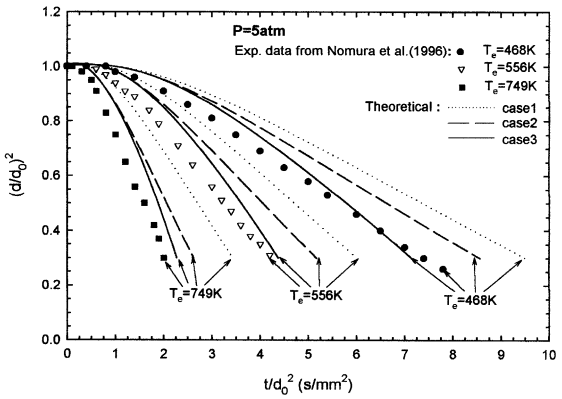

Fig. 4. Theoretical and experimental time variations of normalized squared droplet diameter for different temperatures, $P = 5$ atm. (Cases as in Fig. 3.)

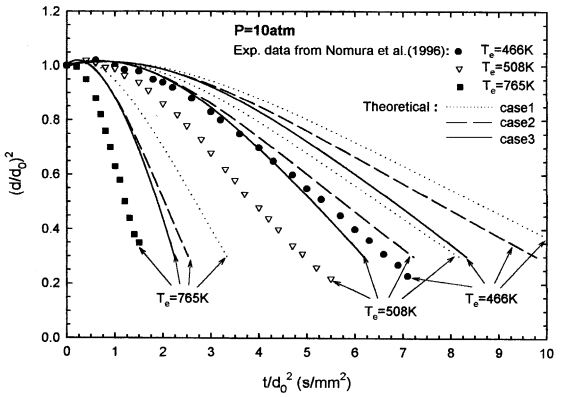

Fig. 5. Theoretical and experimental time variations of normalized squared droplet diameter for different temperatures, $P = 10$ atm. (Cases as in Fig. 3.)

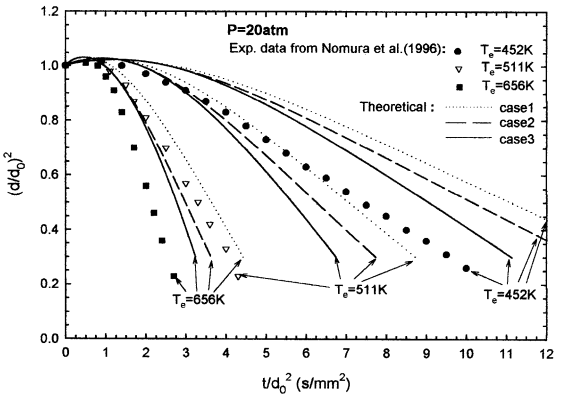

Fig. 6. Theoretical and experimental time variations of normalized squared droplet diameter for different temperatures, $P = 20$ atm. (Cases as in Fig. 3.)

4). For the cases of 10 and 20 atm, mild discrepancies are present even with both effects accounted for. More comparisons are made with the experimental data of Ristau et al. [8] (not shown). Again, the agreement is excellent for $P = 1$ bar and mild discrepancies exist for $P = 10$ bar. This may be partly due to the increasing experimental difficulty and uncertainty with increasing pressure. For example, the experimental data for the case of $T_e = 511$ K and $P = 20$ atm (Fig. 6) are obviously unreliable, because its time variation is inconsistently too rapid with reference to the other cases of 452 and 656 K. In addition, the ranged initial diameter (0.6–0.8 mm) and the required time of 0.16 s to introduce a droplet into the furnace [9] may be secondary causes for the discrepancies. Also, Ristau et al. [8] indicated that part of the discrepancies in their experiments resulted from the uncertain estimation of the droplet diameter due to vibration and the influence of the support fiber. In the theoretical aspect, our model has included the currently most sophisticated considerations for high pressure effects. The correctness has been proven by the experimental phase equilibrium data at supercritical pressure, as discussed earlier. In addition, the reliability of our numerical program has been carefully confirmed by its precise reproducibility of several other published results [8,10,12,14,39]. Furthermore, our simplified calculations have shown that the gas-phase radiative absorption by the fuel vapor contributes only minor improvement of the agreement at high pressures. Therefore, the remaining mild discrepancies at high pressures are less likely attributable to the theoretical insufficiency. Further research work is needed for explanation.

In Fig. 7, the theoretical evaporation rate constants k, defined in Fig. 1(b), are compared with the experimental results for various temperatures and pressures. It is noted from Figs. 3–6 that the slopes of the curves for

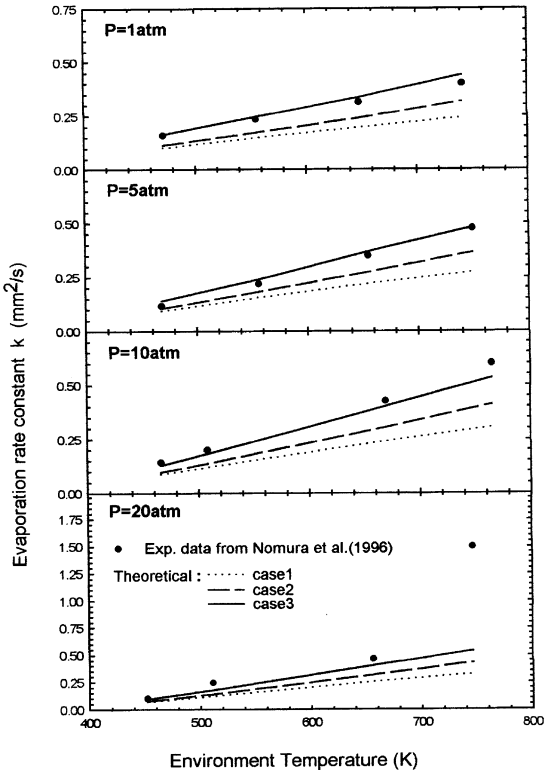

Fig. 7. Theoretical and experimental evaporation rate constant k for different temperatures and pressures. (Cases as in Fig. 3.)

case 3 (including both fiber conduction and radiative absorption) deviate slightly from a constant, due to the variation in the droplet size and its ratio to the fiber size. For the theoretical results, the evaporation rate constants were extracted at $(d/d_0)^2 = 0.5$; for the experimental results, they were determined based on the data points between $(d/d_0)^2 = 0.5$–0.8. While those values of k obtained without considering fiber conduction and radiative absorption are much too small, those with both effects considered match with experiments excellently. (The experimental data for $T_e = 746$ K and $P = 20$ atm are obviously inconsistent with the other data and can be considered unreliable.) Again, the relative importance of radiative absorption increases with increasing temperature.

The time variations of the heat input through different ways are illustrated in Figs. 8 and 9, respectively, for $P = 1$ and 20 atm. In Fig. 8(a) for $T_e = 741$ K and $P = 1$ atm, both effects are strongly manifested. The heat input through radiative absorption gradually decreases with time due to droplet shrinkage, while the contribution through fiber conduction increases with time as the fiber is being heated up. Neglecting both effects leads to a greatly under-predicted total heat input. For a lower temperature, $T_e = 471$ K, the relative amount of the additional heat inputs decreases, especially for the radiative absorption, as shown in Fig. 8(b). At a higher pressure, $P = 20$ atm, the additional heat inputs due to the two effects are also larger for a higher temperature,

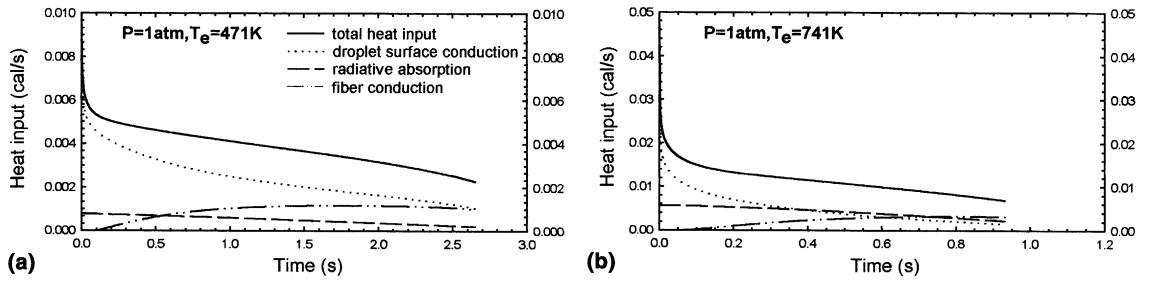

Fig. 8. Transient heat inputs through different ways for two different temperatures, $P = 1$ atm. (Cases as in Fig. 3.)

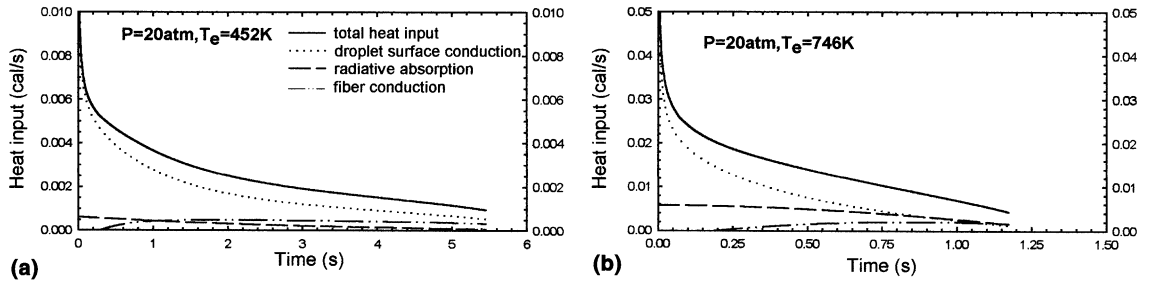

Fig. 9. Transient heat inputs through different ways for two different temperatures, $P = 20$ atm. (Cases as in Fig. 3.)

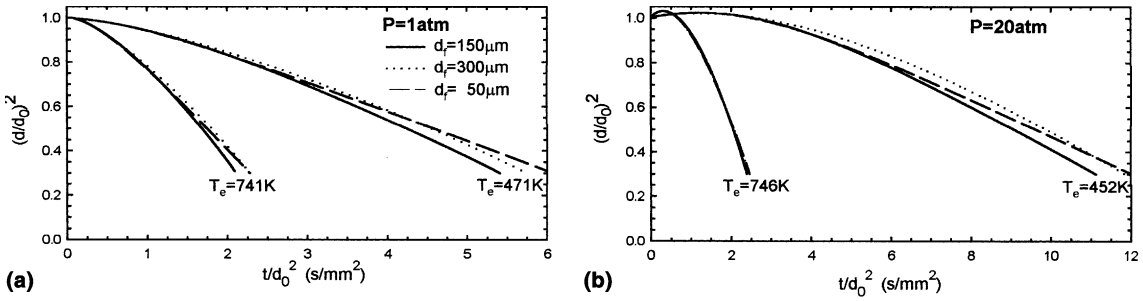

Fig. 10. Fiber conduction effect for different fiber diameters: (a) $P = 1$ atm; (b) $P = 20$ atm.

as shown in Fig. 9. Comparing Fig. 8(a) with Fig. 9(a), or Fig. 8(b) with Fig. 9(b), the proportions of the additional inputs are found to decrease with increasing pressure. This is because the heat input through the conduction on the droplet surface increases significantly with increasing pressure, while those through fiber conduction and radiative absorption change little.

The time-dependence in the fiber conduction input, as shown in Figs. 8 and 9, implies an over-prediction of fiber input by Kadota and Hiroyasu [17], who assumed a steady-state analysis. Also, for the radiative input, Kadota and Hiroyasu adopted $\alpha_{\text{eff}} = 0.49$, which is smaller than our 0.93 and the value of 0.92–0.94 of Lage and Rangel [23]. Consequently, the radiative absorption may be under-predicted by Kadota and Hiroyasu [17].

In Fig. 10, the effect of fiber conduction is theoretically investigated for different fiber diameters ($d_f = 0.05$, 0.15 and 0.3 mm). In the calculations, liquid-phase radiative absorption is included. For different temperatures and pressures, the case with fiber diameter of 0.15 mm exhibits the strongest enhancement of evaporation. It is interesting to find weaker enhancement for $d_f = 0.3$ mm than for $d_f = 0.05$ mm, especially for the early stage. This is because the 0.3 mm fiber heats up slower to result in less axial conduction into the droplet. In addition, the fiber conduction effect grows with time and is stronger for lower temperatures.

10. Concluding remarks

Using a comprehensive droplet evaporation model, with the heat conduction through the support fiber and the liquid-phase radiative absorption of the incident radiation from the furnace wall accounted for, we have obtained remarkably improved agreement with microgravity evaporation experiments for different temperatures (450–765 K) and pressures (1–20 atm). For 1 and 5 atm, the agreement is excellent for the time variation of droplet size for all the temperatures. For higher pressures ($P = 10$ and 20 atm), there are mild discrepancies which may be partly attributed to the high difficulty and uncertainty associated with high-pressure microgravity experiments. As far as the evaporation rate constants k are concerned, the predicted values agree excellently with the experimental data, provided one unreliable high-pressure experimental datum is ruled out. The effects of fiber conduction and radiative absorption are strongly manifested, with the former effect decreasing and the latter increasing with increasing environment temperature. The time variation of the heat inputs through different ways has been investigated. The radiative absorption decreases with time due to droplet shrinkage, and the fiber conduction increases with time as the fiber is being heated up. The relative importance of these additional inputs decreases with increasing pressure because of the increasing heat conduction through the droplet surface. The effect of fiber conduction on the evaporation rate has been compared for three different fiber diameters ($d_f = 0.05$, 0.15 and 0.3 mm). Among them, the case of $d_f = 0.15$ mm presents the strongest enhancement of evaporation.

Acknowledgements

This work was funded by National Science Council, R.O.C. under Contract NSC89-2212-E-007-090.

References

[1] G.M. Faeth, Current status of droplet and liquid combustion, Prog. Energy Combust. Sci. 3 (1977) 191–224.
[2] C.K. Law, Recent advances in droplet vaporization and combustion, Prog. Energy Combust. Sci. 8 (1982) 171–201.
[3] W.A. Sirignano, Fuel droplet vaporization and spray combustion theory, Prog. Energy Combust. Sci. 9 (1983) 291–322.
[4] S.D. Givler, J. Abraham, Supercritical droplet vaporization and combustion studies, Prog. Energy Combust. Sci. 22 (1996) 1–28.
[5] R.L. Matlosz, S. Leipziger, T.P. Torda, Investigation of liquid drop evaporation in a high temperature and high

pressure environment, Int. J. Heat Mass Transfer 15 (1972) 831–852.
[6] H. Hiroyasu, T. Kadota, T. Senda, T. Imamoto, Evaporation of a single droplet at elevated pressures and temperatures, Trans. JSME 40 (339) (1974) 3147–3155.
[7] J.P. Hartfield, P.V. Farrell, Droplet vaporization in a high-pressure gas, Trans. ASME: J. Heat Transfer 115 (1993) 699–706.
[8] R. Ristau, U. Nagel, H. Iglseder, J. König, H.J. Rath, H. Nomura, M. Kono, M. Tanabe, J. Sato, Theoretical and experimental investigations on droplet evaporation and droplet ignition at high pressures, Microgravity Sci. Technol. VI/4 (1993) 223–228.
[9] H. Nomura, Y. Ujiie, H.J. Rath, J. Sato, M. Kono, Experimental study on high-pressure droplet evaporation using microgravity conditions, in: Proceedings of 26th Symposium (Int.) on Combustion, 1996, pp. 1267–1273.
[10] K.C. Hsieh, J.S. Shuen, V. Yang, Droplet vaporization in high-pressure environments I: near critical conditions, Combust. Sci. Technol. 76 (1991) 111–132.
[11] E.W. Curtis, P.V. Farrell, A numerical study of high-pressure droplet vaporization, Combust. Flame 90 (1992) 85–102.
[12] H. Jia, G. Gogos, Investigation of liquid droplet evaporation in subcritical and supercritical gaseous environments, Int. J. Heat Mass Transfer 6 (4) (1992) 738–745.
[13] H. Jia, G. Gogos, High pressure droplet vaporization; effects of liquid-phase gas solubility, Int. J. Heat Mass Transfer 36 (18) (1993) 4419–4431.
[14] T.L. Jiang, W.T. Chiang, Effects of multiple droplet interaction on droplet vaporization in subcritical and supercritical pressure environments, Combust. Flame 97 (1994) 17–34.
[15] A. Umemura, Y. Shimada, Characteristics of supercritical droplet gasification, in: Proceedings of 26th Symposium (Int.) on Combustion, 1996, pp. 1621–1628.
[16] G.S. Zhu, S.K. Aggarwal, Transient supercritical droplet evaporation with emphasis on the effects of equation of state, Int. J. Heat Mass Transfer 43 (2000) 1157–1171.
[17] T. Kadota, H. Hiroyasu, Evaporation of a single droplet at elevated pressures and temperatures, Bull. JSME 19 (138) (1976) 1515–1521.
[18] A.T. Shih, C.M. Megaridis, Suspended droplet evaporation modeling in a laminar convective environment, Combust. Flame 102 (1995) 256–270.
[19] C.T. Avedisian, G.S. Jackson, Soot patterns around suspended *n*-heptane droplet flames in a convection-free environment, J. Propulsion Power 16 (6) (2000) 974–979.
[20] G.A.E. Godsave, Studies of the combustion of drops in a fuel spray – the burning of single drops of fuel, in: Proceedings of 4th Symposium (Int.) on Combustion, 1953, pp. 818–830.
[21] T. Saitoh, K. Yamazaki, R. Viskanta, Effect of thermal radiation on transient combustion of a fuel droplet, J. Thermophys. Heat Transfer 7 (1) (1993) 94–100.
[22] G.M. Harpole, Radiative absorption by evaporating droplets, Int. J. Heat Mass Transfer 23 (1980) 17–26.
[23] P.L.C. Lage, R.H. Rangel, Total thermal radiation absorption by a single spherical droplet, J. Thermophys. Heat Transfer 7 (1) (1993) 101–109.
[24] P.L.C. Lage, R.H. Rangel, Single droplet vaporization including thermal radiation absorption, J. Thermophys. Heat Transfer 7 (3) (1993) 502–509.
[25] K.C. Chiang, J.S. Shieh, Theoretical investigation of transient droplet combustion by considering flame radiation, Int. J. Heat Mass Transfer 38 (14) (1995) 2611–2621.
[26] R.C. Reid, J.M. Prausnitz, B.E. Poling, The Properties of Gases and Liquids, fourth ed., McGraw-Hill, New York, 1987.
[27] M.N. Özisik, Radiative Transfer and Interactions with Conduction and Convection, Wiley, New York, 1973, p. 60 and 255.
[28] A. Tuntomo, C.L. Tien, Optical constants of liquid hydrocarbon fuels, Combust. Sci. Technol. 84 (1992) 133–140.
[29] G.C. Pomraning, C.E. Siewert, On the integral form of the equation of transfer for a homogeneous sphere, J.Q.S.R.T. 28 (6) (1982) 503–506.
[30] S.W. Churchill, H.H.S. Chu, Correlating equations for laminar and turbulent free convection from a horizontal cylinder, Int. J. Heat Mass Transfer 18 (1975) 1049–1053.
[31] C.W. Robert, J.A. Melvin, CRC Handbook of Chemistry and Physics, 61st ed., Boca Raton, FL, 1981, p. F-80.
[32] R.W. Hakinson, G.H. Thomson, A new correlation for saturated densities of liquids and their mixtures, AIChE J. 25 (4) (1979) 653–663.
[33] G.H. Thomson, K.R. Brobst, R.W. Hakinson, An improved correlation for densities of compressed liquids and liquid mixtures, AIChE J. 28 (4) (1982) 671–676.
[34] T.E. Daubert, R.T. Danner, Physical and Thermodynamic Properties of Pure Chemicals, Data Compilation, Hemisphere, NY, 1989.
[35] L.I. Stiel, G. Thodos, The thermal conductivity of nonpolar substances in the dense gaseous and liquid regions, AIChE J. 10 (1) (1964) 26–31.
[36] M. Yorizane, S. Yoshimura, H. Masuoka, H. Yoshida, Thermal conductivities of binary gas mixtures at high pressures: N_2–O_2, N_2–Ar, CO_2–Ar, and CO_2–CH_4, Ind. Eng. Chem. Fundam. 22 (1983) 458–463.
[37] B.K. Lee, M.G. Kesler, A generalized thermodynamic correlation based on three-parameter corresponding states, AIChE J. 21 (3) (1975) 510–527.
[38] S. Takahashi, Preparation of a generalized chart for the diffusion coefficients of gases at high pressures, J. Chem. Eng. Jpn. 7 (6) (1974) 417–420.
[39] G.L. Hubbard, V.E. Denny, A.F. Mills, Droplet evaporation: effects of transients and variable properties, Int. J. Heat Mass Transfer 18 (1975) 1003–1008.